

# Comb-calibrated solar spectroscopy through a multiplexed single-mode fiber channel

R A Probst<sup>1</sup>, L Wang<sup>2,3</sup>, H-P Doerr<sup>4</sup>, T Steinmetz<sup>5</sup>,  
T J Kentischer<sup>4</sup>, G Zhao<sup>2</sup>, T W Hänsch<sup>1</sup>, Th Udem<sup>1</sup>,  
R Holzwarth<sup>1,5</sup> and W Schmidt<sup>4</sup>

<sup>1</sup>Max-Planck-Institut für Quantenoptik, Hans-Kopfermann-Str. 1, 85741 Garching, Germany

<sup>2</sup>Key Laboratory of Optical Astronomy, National Astronomical Observatories, Chinese Academy of Sciences, A20 Datun Road, Beijing 100012, China

<sup>3</sup>Universitäts-Sternwarte München, Scheinerstr. 1, 81679 München, Germany

<sup>4</sup>Kiepenheuer-Institut für Sonnenphysik, Schöneckstr. 6, 79104 Freiburg, Germany

<sup>5</sup>Menlo Systems GmbH, Am Klopferspitz 19a, 82152 Martinsried, Germany

E-mail: rafael.probst@mpq.mpg.de

**Abstract.** We investigate a new scheme for astronomical spectrograph calibration using the laser frequency comb at the Solar Vacuum Tower Telescope on Tenerife. Our concept is based upon a single-mode fiber channel, that simultaneously feeds the spectrograph with comb light and sunlight. This yields nearly perfect spatial mode matching between the two sources. In combination with the absolute calibration provided by the frequency comb, this method enables extremely robust and accurate spectroscopic measurements. The performance of this scheme is compared to a sequence of alternating comb and sunlight, and to absorption lines from Earth's atmosphere. We also show how the method can be used for radial-velocity detection by measuring the well-explored 5-minute oscillations averaged over the full solar disk. Our method is currently restricted to solar spectroscopy, but with further evolving fiber-injection techniques it could become an option even for faint astronomical targets.

*Keywords:* frequency combs, astronomy, solar physics

## 1. Introduction

Laser frequency combs (LFCs) have revolutionized precision spectroscopy in atomic and molecular physics [1], enabling measurements of transition frequencies with unprecedented accuracy. Recently, they have grown into high-precision frequency calibrators for astronomical spectrographs [2–10]. An LFC represents an absolute optical frequency reference, directly linked to an accurate radio-frequency (RF) standard such as an atomic clock. Its spectrum consists of a very regular series of sharp lines (or modes) at frequencies

$f_n = f_0 + n f_r$ , where the repetition frequency  $f_r$  is the mode spacing, the offset frequency  $f_0$  is a global shift of the mode structure, and the mode number  $n$  is an integer.  $f_r$  and  $f_0$  are both radio frequencies, accessible to conventional electronics, while the values of  $n$  are high enough (from about 80 000 to 120 000 for the LFC described in this work) to enable the transfer from RF to optical frequencies. With its unique properties, the LFC comes close to an ideal calibrator for spectrographs [2], whose outstanding accuracy is expected to open up new perspectives in astronomy. This comprises the detection of Earth-like extrasolar planets by measuring the recoil motion of their host stars [9]. LFCs may also enable a direct measurement of the acceleration of the cosmic expansion [11], and a more accurate cosmological search for variability of fundamental constants [12].

A central aspect in precision astronomical spectroscopy is the measurement of radial-velocity (RV) changes of celestial bodies via Doppler shifts of spectral lines. With conventional calibration techniques, the best spectrographs are currently limited to an RV precision of roughly 1 m/s over large time spans. LFCs hold promise to enable RV measurements at an accuracy of 1 cm/s over arbitrary time horizons, and a 2.5 cm/s calibration repeatability has already been demonstrated on a time scale of hours [9]. Unlike other calibration sources, LFCs are not only repeatable, but to the same degree also accurate, i.e. they allow assigning wavelengths, or optical frequencies, that come close to the true values. Most applications would profit from LFCs mainly for their high repeatability, but the high accuracy of LFCs can also be beneficial, e.g. to compare spectra from different instruments. This property has also been exploited by [10] to create an improved atlas of the solar lines in the visible.

Current high-precision spectrographs are usually connected to their telescopes via optical fibers, to detach them from telescope guiding, increasing the stability of the measurements. The spectrographs are usually equipped with a second fiber channel that is used to simultaneously calibrate the spectrograph during each measurement, to track spectrograph drifts. Differential drifts between the two channels are minimized by a rigid mechanical connection between the fiber outputs. However, since it is challenging to couple light from astronomical objects efficiently into single-mode fibers (SMFs), current high-precision spectrographs are fed with multimode fibers. While an SMF guides only a single, approximately Gaussian shaped beam profile, a multimode fiber supports a variety of beam profiles. The profile at the output of a multimode fiber depends on the beam alignment at its input, and therefore on telescope guiding. This translates into uncertainties in RV measurements.

In this work, the use of SMFs for LFC-based calibration of astronomical spectrographs is explored. The tests presented here have been made at the Vacuum Tower Telescope (VTT), a solar telescope in Tenerife, Canary Islands, that is operated by the KIS. The very high optical powers available from the Sun allow the use of SMFs to feed the spectrograph both with sunlight and comb light, tolerating low coupling efficiencies on the part of the Sun. However, advances in adaptive optics are anticipated to enable efficient SMF coupling

of distant stars [13], making our approach interesting for night-time astronomy as well. As an alternative to adaptive optics, photonic lanterns have recently been developed as efficient multimode to single-mode converters for astronomical applications [14, 15]. They split up the light of a multimode fiber into an array of SMF channels. The use of SMFs fully decouples the spatial beam parameters in the spectrograph from telescope guiding, which potentially limits the precision of other fiber-fed spectrographs. SMFs also eliminate the degradation of the beam profile through formation of laser speckles upon fiber coupling of coherent light. For multimode fibers, this occurs due to modal interference. This point is particularly critical for the LFC, owing to its high degree of coherence.

Another concept that we introduce for spectrograph calibration with an LFC is multiplexing of the fiber channel, which involves coupling both comb and sunlight into one single fiber. We investigate both temporally separated and simultaneous fiber injection of the two sources. Especially the latter concept is shown to enable very accurate tracking of spectrograph drifts during measurements. This eliminates the need for an extra fiber for calibration, that can potentially drift versus the other one and thereby cause calibration errors. In combination with the use of SMFs, we obtain nearly perfect spatial mode-matching between comb and sunlight, and thus an extremely robust calibration. This is similar to the mode in which iodine absorption cells are operated, which however absorb a part of the science light, and are surpassed by LFCs in a number of calibration characteristics such as accuracy, repeatability, and spectral coverage.

We demonstrate our methodology by observing the 5-minute oscillations in the integrated solar spectrum, i.e. in the spectrum averaged over the full solar disk. These oscillations are well understood [16] and have been extensively characterized [17–19]. They hence represent a suitable test-bed for our method. The observation of integrated sunlight, considering the "Sun-as-a-star", is of great interest for night-time astronomy, as it allows investigating effects like stellar activity on RV detection. These studies could not be carried out in such detail on other stars, but are needed for a more accurate search for extrasolar planets. Of course, our method is not limited to integrated sunlight, and the VTT telescope allows placing the SMF tip in the image of the Sun. This results in spatially resolved, comb-calibrated measurements, supported by the adaptive optics of the VTT. Currently, this approach is being used to study the center-to-limb variation of the solar convective blue shift, and is proposed for characterization of the solar meridional motion [7].

## **2. Instruments and observations**

The observations described and analyzed in this work were made at the VTT in Tenerife [20], where an infrared LFC had already been tested in 2008 [3]. For our tests, we fed the VTT echelle spectrograph with integrated sunlight from the auxiliary full-disk telescope ChroTel [21, 22], located in the same building as the VTT telescope. Within the beam path of the ChroTel, we installed a lens that produced an about 4 mm wide image

of the pupil of the telescope, in which we placed the tip of an SMF with a 2.5  $\mu\text{m}$  core diameter. The lens roughly matched the numerical aperture (NA) of the sunlight to the fiber NA of 0.13. This resulted in 800 nW of visible sunlight coupled into the SMF, which corresponds to a coupling efficiency of 0.1 ppm with respect to the total solar radiation power collected by the telescope. The fairly low coupling efficiency is mainly due to the fact, that to an earthbound observer the Sun – unlike other stars – appears as an extended source with poor spatial coherence properties. Its light thus consists of a multitude of spatial modes without a well-defined relative phase. Only one of these modes can be fully matched, and thereby efficiently coupled, to the single spatial mode of an SMF at a time. The sunlight collected by the ChroTel consists of several million spatial modes, as can be deduced from its optical resolution. This necessarily entails a poor spatial mode overlap of the guided mode of the SMF with the incident light field at the pupil image. The problem could be circumvented by coupling each spatial mode to a different SMF, e.g. with a photonic lantern, but in our case this is impractical because of the great number of spatial modes. This is different for distant stars, where photonic lanterns should represent a viable solution. Further, a diffraction limited image of a distant star, e.g. obtained by employing adaptive optics, could enable coupling into an SMF with efficiencies of  $>70\%$  [13].

The SMF in this setup collects light from every point of the solar disk, but not with equal efficiency, owing to the approximately Gaussian-shaped acceptance profile of the SMF. This is because in the pupil image, light from different locations on the Sun is incident from different angles. As a result, the observed solar spectrum represents a weighted average over the solar disk. The rotation of the Sun imprints a  $\pm 2$  km/s RV variation across the solar disk. Inaccurate telescope guiding can consequently distort the RV measurement, by shifting the centroid of the weighted spatial average towards the blue or red-shifted region. The specified guiding accuracy of 0.5 arcsec of the ChroTel should keep the resulting RV errors below approximately 1 m/s. This guiding accuracy can however only be guaranteed under sufficiently good observation conditions. It is also important to note, that this sort of RV error from telescope guiding would not exist, if the technique was used in stellar night-time astronomy, since distant stars are normally not spatially resolved.

The LFC as installed at the VTT in October 2011 is described in [7]. In May 2012, just before making the tests reported here, the system was upgraded to enable higher calibration accuracy and more reliable operation [8]. The system is referenced to a GPS disciplined quartz oscillator, accurate within a fractional uncertainty of  $< 10^{-12}$  for integration times exceeding 1 s. It features a broadband visible output coupled into an SMF, and routinely delivers sufficient power for spectrograph calibration over a 460–680 nm spectral range. It was operated at a repetition frequency of  $f_r = 5.445$  GHz and an offset frequency of  $f_0 = +100$  MHz. This comb spectrum is synthesized from an LFC with initially smaller mode spacing, by suppressing unwanted modes with a series of Fabry-Pérot filters [23]. It is estimated, that the unwanted modes are suppressed to better than 47 dB, and thus cannot shift the calibration by more than 5 kHz [24]. At a center wavelength of 630 nm, as used in

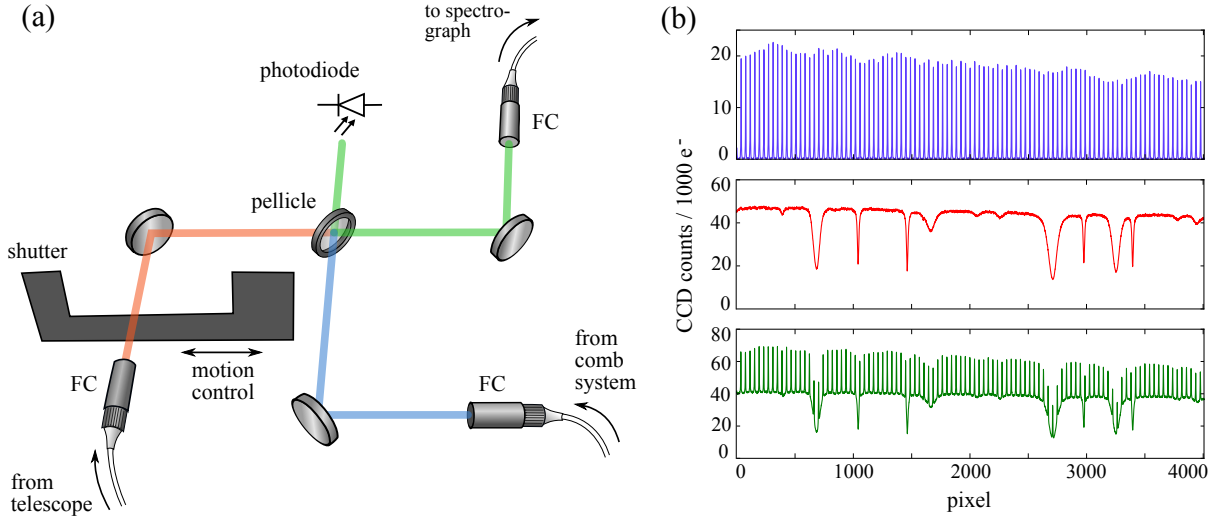


**Figure 1.** (a) Setup of the optical multiplexer: The sunlight (red) from the telescope and the comb light (blue) enter the free-space section through fiber collimators (FC). They are combined (green) on a pellicle beam splitter, and then coupled into the output fiber leading to the spectrograph. The shutter can be positioned to block either the sunlight, the comb light, neither, or both. Three silver mirrors inside the beam path support optical alignment. (b) Spectra as measured using the VTT spectrograph at different positions of the shutter, with the multiplexer transmitting only comb light (top), sunlight (center), or both (bottom).

this work, this corresponds to 3 mm/s. Furthermore, owing to the finite width of the comb modes, the mode filtering can shift their center of gravity by skewing their shape, in case the filter transmission peaks are not perfectly centered at their position [25]. In analogy to the discussion in [26] we estimate, that this effect can cause line shifts of up to 2.1 cm/s for this LFC.

The sunlight from the telescope and the calibration light from the LFC are combined into a one SMF by an optical multiplexer that is shown in figure 1(a). The fiber-coupled comb and sunlight enter the free-space section of the multiplexer through fiber collimators using achromatic triplet lenses. The two beams are overlapped on a 2  $\mu\text{m}$  thick uncoated pellicle, that on average reflects 8 % of the comb light and transmits 92 % of the sunlight. The reflectivity (and transmittance) is modulated by interferences on the two surfaces of the pellicle. Its very low thickness stretches the period of the modulation to much larger than the observed spectral range of 0.7 nm (see below). Another solution would be to replace the pellicle by a wedged glass plate, to suppress the modulation. The combined beam of comb and sunlight is coupled into an SMF leading to the spectrograph. All fibers are identical, feature single-mode guidance from 450 to 680 nm, and use connectors with angled end facets. The pellicle produces a second overlapped output, which for alignment purposes is monitored on a photodiode. Within the free-space section, there is a beam shutter in

form of a U-shaped black metal panel, whose position is controlled with a motorized linear translation stage. Four positions for the shutter are defined, in which it blocks either the beam from the Sun, that of the comb, neither, or both.

The output fiber of the multiplexer leads to the VTT echelle spectrograph. From there, the light is focused through the entrance slit of the spectrograph by an aspheric lens, that matches the NA of the beam to that of the spectrograph. The VTT spectrograph has a very high resolution of  $R = 10^6$ , but usually only observes a single echelle order at a time, and hence only a rather narrow spectral range. The center wavelength of the observation can be tuned over a wide range by adjusting the angles of the echelle grating and predisperser. The image plane of the spectrograph can be accessed freely, allowing to place and exchange CCD cameras as desired by the user. With the PCO 4000 camera that we used to record our spectra, we could observe a 0.7 nm wide spectral range that we centered at 630.0 nm. The CCD chip of the camera was cooled down to  $-18^\circ\text{C}$ , had a root-mean-square (RMS) readout-noise of 11 photoelectrons, and counted 3.3 photoelectrons for every step of the 14 bit readout amplifier. The CCD had a  $9\ \mu\text{m} \times 9\ \mu\text{m}$  pixel pitch with 4008 pixels in the dispersion direction of the echelle order and 2672 pixels perpendicular to it. We employed an 8-to-1 hardware binning of the pixels in the latter direction. Along the illuminated pixels, we summed up 5 of the binned pixels in every column perpendicular to the dispersion direction, in order to gain a 1-dimensional data string from the CCD image.

For all exposures, we chose an exposure time of 1000 ms. The position of the shutter within the multiplexer was changed periodically for the observations, to first record a spectrum with comb light only, then with sunlight only, and finally with both, after which the cycle was repeated (see figure 1(b)). Between the exposures, we left a 1000 ms pause for the shutter to move. With this choice of the exposure cycle, two different multiplexed calibration schemes can be put into practice: If only the frames with pure sunlight or pure comb light are considered, the solar spectrum can be calibrated by interpolating the calibrations obtained from the comb exposures directly before and directly after each Sun exposure. This temporally separated signal transmission is known as time-division multiplexing. We refer to this calibration scheme as time-interlaced calibration. If also the exposures containing both comb and sunlight are considered, the solar spectra can be calibrated from the overlaid comb. This concept is hereafter referred to as overlaid calibration. In the following sections we investigate the benefits and drawbacks of the two calibration schemes, and assess their performance.

The observations used for our analysis were made on May 29, 2012, from 12:18 to 17:16 coordinated universal time (UTC). During this time span, 2715 full cycles as described above were recorded. Unfortunately, the series was interrupted several times due to technical problems, and the telescope guiding was partly disturbed by passing clouds. Towards the end of the series, 86 minutes of uninterrupted operation with stable guiding were accomplished, which we use as our observed sample for the comb-Sun comparisons. However, to test the stability of the comb calibration on its own, all recorded comb spectra

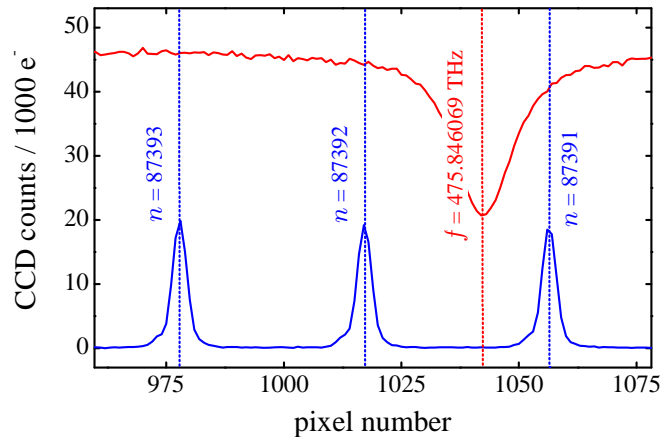


**Figure 2.** Identification of comb lines. The graph shows a small portion of the comb spectrum (blue solid line near bottom) and of the solar spectrum (red solid line near top). The mode numbers  $n$  of the comb lines at the positions indicated by the blue dashed lines are derived from the known frequency  $f$  of a telluric  $O_2$  line (red dashed line).

are usable. The observed solar spectrum also contained several  $O_2$  lines of telluric origin, i.e. stemming from Earth’s atmosphere. Their line centers are independent of telescope guiding, and hence to compare the LFC with these lines, all recorded solar spectra are of use.

### 3. Calibration tests

#### 3.1. Spectrograph calibration

The known offset frequency and mode spacing of the comb allow to attribute absolute frequencies to the observed comb lines, as soon as they have been assigned mode numbers. The latter can be derived from the known frequencies of the lines in the observed solar spectrum. The telluric  $O_2$  lines are particularly well suited for this task, because they are fairly deep and much more narrow and stable than lines originating from the solar photosphere. Their frequencies are listed in the HITRAN database [27], which we use to attribute mode numbers to the comb lines as shown in figure 2. The result is that the 101 observed comb lines have mode numbers ranging from 87 417 to 87 317.

As a next step, the comb lines are fitted with Gaussian functions using the Levenberg-Marquardt algorithm [28] (see figure 3(a)). The fit algorithm delivers uncertainties of the line centers from error propagation of the photon noise at each data point. The photon noise is assumed to be  $[|N| + (R)^2]^{1/2}$ , where  $N$  denotes the number of detected photoelectrons, and  $R$  the CCD readout noise. Subtraction of the dark and bias current of the CCD is included in  $N$ , as well as correction for different sensitivity of adjacent pixels (flat fielding). The centers of the fitted lines and their uncertainties are the basis for further analysis.

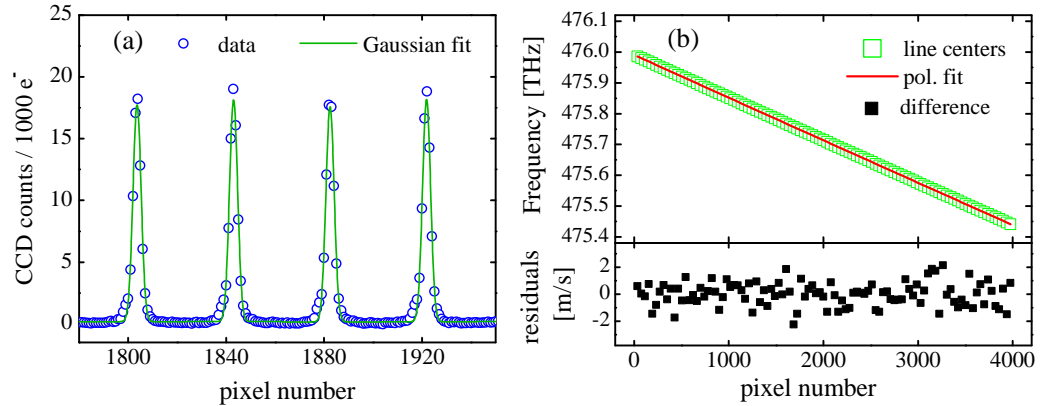


**Figure 3.** (a) Small section of the observed comb spectrum, with a Gaussian function fitted to each comb line. The centers of the fitted Gaussians are assumed as the centers of the comb lines on the CCD. (b) Upper plot: Frequencies of the observed comb modes versus their line centers on the CCD. The data points are approximated by a third-order polynomial. Lower plot: Fit residuals, converted into m/s. Root-mean-square (RMS) of the fit residuals: 0.87 m/s. Photon noise: 0.60 m/s.

The fact that the observed line profiles are not exactly Gaussian is uncritical for the further analysis, which merely requires a precise definition of the line center that leads to reproducible results.

An absolute calibration can be obtained from the line centers on the CCD and the known frequencies of the corresponding comb modes. With this information, the pixel-to-frequency relation can be mapped across the CCD, which is approximated by a third-order polynomial (figure 3(b)). According to the fitted polynomial, which is hereafter referred to as the frequency solution, an average CCD pixel spans 138.2 MHz or 87.09 m/s. The RMS deviation of the fit residuals of 0.87 m/s is close to the photon noise limit of 0.60 m/s, but the discrepancy still requires an explanation. Using a higher-order polynomial for fitting does not significantly reduce the discrepancy. In [4], remarkable deviations of the comb line centers from the frequency solution were observed, and attributed to irregularities of the pixelation caused by the manufacturing process of the CCD. In particular, abrupt changes of the pixel-to-frequency relation were found to occur every 512 pixels, which is equal to the width of the mask used for fabrication. In our case, the deviations are far less severe and do not display an obvious, periodically occurring pattern. However, after averaging the residuals from the frequency solution over all (>2700) comb spectra, their RMS still amounts to 0.50 m/s. Hence, the deviations above photon noise seem to be largely reproducible and of systematic nature. We thus attribute the largest portion of these deviations to irregularities in the CCD pixelation, even though the CCD was apparently not stitched together from smaller lithographic blocks of pixels, which is clearly preferable.



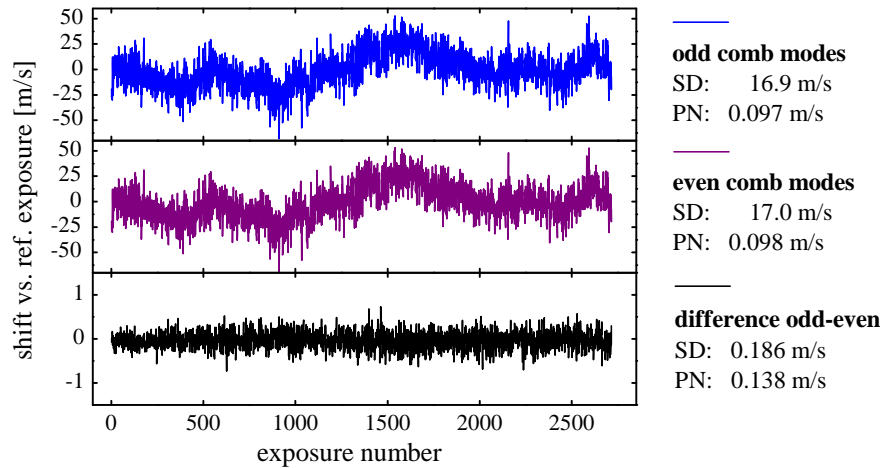


**Figure 4.** Test of the calibration repeatability for overlaid calibration. The calibration shifts of two subsets of modes are compared, one formed by the lines with odd mode numbers (upper plot), and the other one formed by the lines with even mode numbers (central plot). The differential calibration shifts between the two subsets are shown in the lowest plot (notice the different vertical scale there). Next to each plot, the standard deviation (SD) and the photon noise limit (PN) of the series are quoted. Integration time: 1 s. Cadence: 1 frame every 6 s.

### 3.2. Calibration repeatability

To assess the calibration repeatability that the LFC provides in different calibration schemes, we consider only exposures with pure comb light, circumventing any limitations from the solar observation.

For testing the calibration repeatability provided by the aforementioned concept of an overlaid calibration, the observed comb lines are divided into two groups: One group is represented by the modes with odd mode numbers, and the other one by even mode numbers. We thus decompose the LFC into two interleaved combs with twofold mode spacing, and assess their relative stability. This mimics an overlaid calibration, with light from two sources simultaneously sent through the same fiber. For each exposure, we compute the shift of the comb lines relative to their position in a reference exposure, which is the first exposure of the series. The combined shift of all odd (even) modes is computed for every exposure by averaging the individual line shifts. The averaging of lines applies photon noise weighting, which means that each line is weighted by its inverse variance given by photon noise. Figure 4 shows the result for the odd modes, the even modes, and the difference between the two. While the shifts of the odd modes and the even modes mainly reflect spectrograph drifts, the difference between the two should not be larger than photon noise, if the two calibrations are consistent to that level. The standard deviation of both the odd and the even modes amounts to 17 m/s, whereas the standard

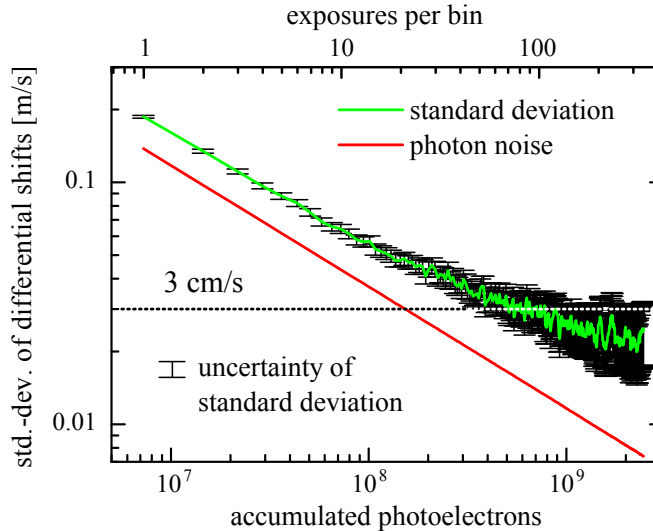


**Figure 5.** Improvement of the calibration repeatability for overlaid calibration with increasing number of accumulated CCD counts. The number of counted photoelectrons is increased by summing up exposures into bins of increasing size (from just 1 exposure per bin to up to 360). The standard deviation (green line) of the differential shifts between odd and even comb modes is computed for each series of binned exposures. The uncertainty of the standard deviation (black error bars) increases with increasing number of accumulated counts because of the decreasing number of bins within the series. An exposure of 1 s was taken once every 6 s.

deviation of the difference is only of 0.186 m/s (photon noise: 0.138 m/s).

The deviation from photon noise limited statistics of the differential shifts, unlike in the case of the deviations from the frequency solution, can hardly be explained by some type of systematic uncertainty. Rather, we conclude that the scatter above photon noise is due to an excess noise source. Thermal noise certainly contributes to the excess noise, since the CCD was not cooled down to the very low temperatures reached by other astronomical CCDs (typically  $-90\text{ }^{\circ}\text{C}$  to  $-120\text{ }^{\circ}\text{C}$ ). The largest portion of the excess noise is however most likely to be provoked by internal seeing within the spectrograph beam path, due to convection of air. The convection elements have different air temperature, and therefore different refractive index, which disturbs the beam. This occurs because the VTT spectrograph is neither evacuated nor thermally stabilized. Nevertheless, for this calibration scheme, the improvement over the passive stability of the spectrograph amounts to about two orders of magnitude.

Even if the calibration repeatability obtained in a single exposure is limited by noise, it can still be further enhanced by combining several exposures into one. If an effect cannot be averaged down in this manner, it means that its influence displays some systematic behavior instead of being purely random. We test this by combining a given number of subsequent exposures into bins. We then carry out the same analysis as previously for

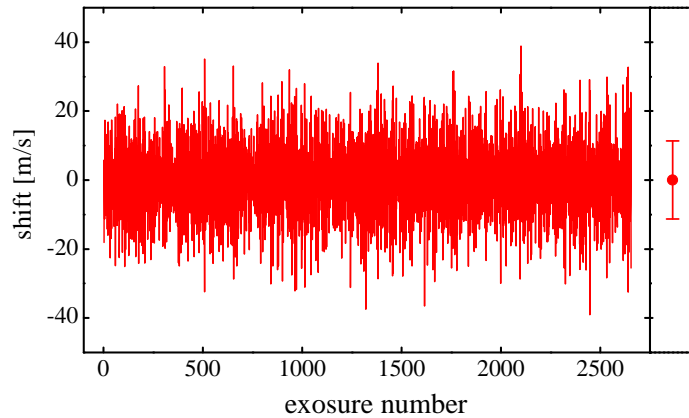


**Figure 6.** Test of the calibration repeatability for time-interlaced calibration. Each calibration is compared to the interpolation of the preceding and subsequent one. The photon-noise weighted difference yields the calibration shifts as shown by the line plot. The error bar on the right represents the standard deviation of 11.3 m/s of the measured shifts. The photon noise limit is 0.097 m/s. Integration time: 1 s. Cadence: 1 frame every 6 s.

the series of binned exposures. The result as a function of bin size is shown in figure 5. The standard deviation drops below 3.0 cm/s for bins of  $>126$  exposures. Again, the photon noise limit is not reached, which would allow an uncertainty as low as 1.2 cm/s at this point. The standard deviation seems to form a plateau near 2.3 cm/s. Strikingly, a plateau at approximately the same value was also found with an LFC on the two-channel spectrograph HARPS [9]. As one of the world’s most stable spectrographs, HARPS is passively stable to better than 1 m/s over at least many hours [29]. The VTT spectrograph in contrast, being neither evacuated nor temperature or pressure stabilized, can drift by up to 100 m/s over a day. The results thus show that with science light and calibration light simultaneously sharing the same spatial mode, spectrograph stabilization is of reduced importance, provided that seeing within the spectrograph is kept low enough.

We now turn to the repeatability as determined for time-interlaced calibration. In this calibration scheme, a science exposure is preceded and followed by a calibration exposure. From the two calibration exposures, two frequency solutions are derived, that are interpolated to calibrate the science exposure. To test this concept with comb light only, each calibration exposure is compared to the interpolation of the calibrations 6 s before and 6 s after it. The total calibration shift is computed as the photon-noise weighted average shift of the lines versus the interpolated calibration. The result is shown in figure 6. It displays a standard deviation of the calibration shifts of 11 m/s, which is only a rather modest improvement over the 17 m/s as obtained when considering the fully uncompensated spectrograph drifts (see upper two plots of figure 4). The uncertainties in this calibration scheme are known to arise from spectrograph drifts that occur on a sub-second time scale [8].

We expect a slightly better repeatability than demonstrated here for the calibration of the solar spectra, because of the twofold lower time span between the interpolated calibration exposures. Generally, the higher the frame rate, the better is the repeatability that we expect for this calibration scheme, as shown in [8] using a 10 Hz frame rate.

## 4. Calibrating solar spectra

### 4.1. Fitting procedures and noise limitations

We now show how our calibration methods can be applied to solar spectra. At first, we only consider exposures containing pure sunlight. The line centers of the absorption lines are determined by fitting, similar to what was done in section 3.1 for the comb lines. We approximate the solar lines with Gaussian functions, and the telluric lines with Lorentzian functions. Contrary to the analysis of the comb exposures, we do not perform the fit on a line-by-line basis, but fit the sum of the functions of all lines. The overall signal level is not constant along the echelle order, which is mainly because of the blaze function of the spectrograph grating. This is modeled by multiplying the sum of functions by a fourth-order polynomial, whose coefficients are adjusted by the fit. The result is shown in figure 7.

The positions of the line centers obtained in this way can be converted into frequencies using the frequency solution obtained from time-interlaced calibration. This permits to track frequency changes (or RV changes) of the lines. Fitting a line model that accurately reflects the true line shapes is not needed here, since we are not interested in an accurate determination of absolute line frequencies. If the absolute frequency of a solar line needs to be specified, it is customary to determine its bisector, to account for the asymmetry of the line profile.

Determining line shifts in the overlaid exposures proves to be considerably more difficult. Here it is a strict necessity that the fit functions accurately reflect the true line shapes. This is not only the case for the solar lines, but for all lines, including the comb lines. If the model used for fitting does not fully match the measured lines, the fit residuals can influence the fit of the overlaid lines, and distort their measured line center. Since the relative signal strength of the two overlaid sources is not fixed, but can vary widely, the crosstalk between the two channels is not stable. Only if the fit functions perfectly match the measured line shapes can it be excluded, that the two fits influence one another in a systematic way. However, the two overlaid spectra will always be affected by each other's photon noise: The added photons from the comb bring in additional noise to the solar spectrum, but do not increase the signal of solar spectrum. Thus, the overlaid calibration usually comes at the price of decreasing the signal-to-noise ratio of the spectrum to be calibrated, and also the calibration itself is affected by a degraded signal-to-noise.

Because the line profiles have to be modeled so accurately, the approach of fitting

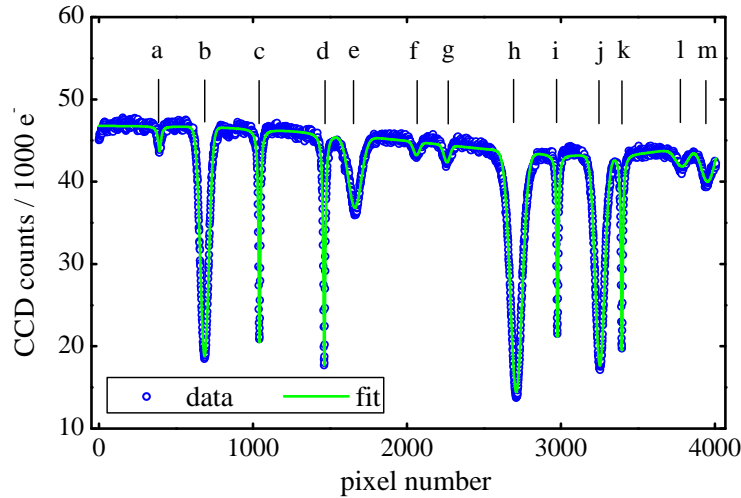


**Figure 7.** Fit of the solar spectrum. The solar lines are fitted with Gaussian functions, while the telluric lines are fitted with Lorentzian functions. The global descent of the signal level from left to right is approximated by a fourth-order polynomial. The black dashes indicate the positions of fitted spectral lines labeled with the identifiers from table 1.

simple mathematical functions to the spectral lines is given up when it comes to analyzing overlaid spectra. Instead, we use template spectra (as described below) for the Sun and for the comb, whose sum (including an offset) is used to approximate the overlaid spectra. The sum of the two templates is matched to the overlaid spectra by shifting each template's position relative to the CCD pixels and by scaling its signal level. The square-sum of the fit residuals ( $\chi^2$ ), applying photon noise weighting of the data points, is calculated by evaluating the templates at the positions of the pixels using cubic spline interpolation. The fit is designed such that the comb lines are scaled individually, since their relative signal strength is also subject to slight changes. Only a selected region around each line in the solar spectrum is fitted at a time. In this manner, lines in the solar spectrum can be tracked separately. Especially the telluric lines are expected to experience shifts that are quite different from the lines of solar origin. They also change in depth over the course of the day, owing to the varying air-mass along the line of sight.

In a first approach, a single comb exposure and a single solar exposure were used as templates for fitting. This however resulted in a very inaccurate localization of the line centers. The reason is, that if a noisy model is fitted to a noisy data set, the resulting  $\chi^2$  as a function of the fit parameters acquires finely structured noise, and thus loses its smoothness. This creates numerous local minima in the  $\chi^2$  landscape for the fit algorithm to get stuck in. The effect was found to be most pronounced for the broad solar lines, because their shallow slopes of the  $\chi^2$  valley can more easily acquire local minima through noise. For the comb, the effect turned out to be close to negligible, because of its narrow

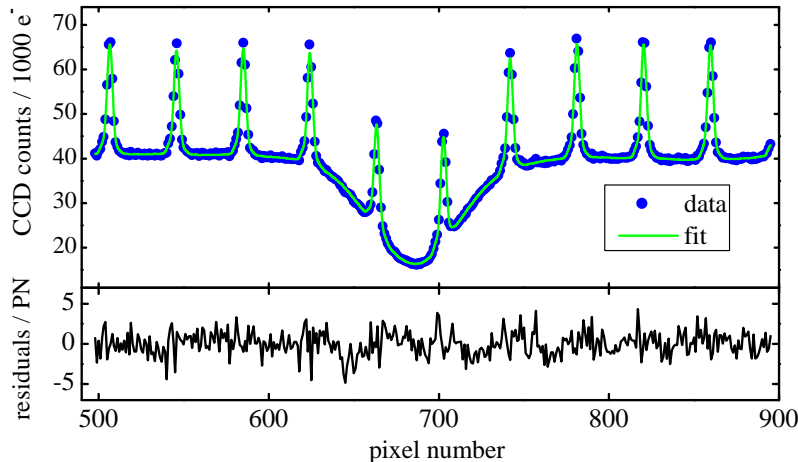


**Figure 8.** Fit of a combined Sun and comb spectrum around a Fe I solar line. Upper plot: The measured data are fitted with a sum of templates for the solar spectrum and for the comb spectrum. Lower plot: Difference between measured data and model fit, expressed in terms of the photon noise (PN) of the data. The root-mean-square (RMS) of the distribution should be 1 if the model fits the lines within the limits given by the photon noise. The actual RMS of the fit residuals is 1.47 times the photon noise.

and numerous lines.

It was thus found to be essential to create templates with minimized noise. We therefore averaged the Sun and comb templates over all available comb and solar spectra. Each spectrum was shifted to match the line centers as indicated by the Gaussian/Lorentzian fits, before including it into the average. This was done separately for every line in the solar spectrum. In order to suppress the noise ever further, the templates for the lines in the solar spectrum were low-pass filtered by a fast-Fourier transform (FFT) filter. The cut-off of the filter had to be adjusted carefully depending on the line width, in order to achieve optimal noise suppression while still fully preserving the line shape. This yielded extremely smooth line templates especially for broad solar lines, where the noise suppression is most critical. Due to the narrow line width of the comb lines, the noise filter was neither applicable nor needed for the comb.

Figure 8 shows the fit and its residuals for a solar Fe I line. The quality of the fit can be judged from the distribution of the fit residuals normalized to the photon noise. The RMS of the residuals is 47 % above the photon noise of the data points, which is about equal to the usual level of excess noise, that was already observed and discussed in section 3. The method therefore fulfills our expectations. All exposures with combined comb and sunlight are analyzed in this way to track the lines in the solar spectrum with respect to the overlaid comb.

A theoretical performance limitation is the photon noise of the solar lines. Even though the photon noise can always be reduced by collecting more exposures, it is useful to estimate

**Table 1.** Photon noise of the fitted line centers in the solar spectrum. PN: Photon noise without overlaid comb. PN2: Photon noise with overlaid comb. The increase of photon noise induced by the overlay is listed in the rightmost column.

identifier	species	origin	PN [m/s]	PN2 [m/s]	increase
a	H <sub>2</sub> O	telluric	20.80	23.08	11 %
b	Fe I	solar	3.17	3.68	16 %
c	O <sub>2</sub>	telluric	1.70	1.74	2 %
d	O <sub>2</sub>	telluric	1.57	1.62	3 %
e	Si I	solar	14.09	15.97	13 %
f	O I / Ni I	solar	58.73	67.83	16 %
g	Sc II	solar	38.92	45.33	16 %
h	Fe I	solar	3.26	3.58	10 %
i	O <sub>2</sub>	telluric	1.94	2.23	15 %
j	Fe I	solar	3.51	3.86	10 %
k	O <sub>2</sub>	telluric	1.79	1.83	2 %
l	Fe I	solar	53.33	56.61	6 %
m	Ti I	solar	31.98	35.92	12 %

the photon noise of the lines in a single exposure with the two calibration schemes. To this aim, we employ Monte-Carlo simulation, adding simulated photon noise to our templates for the solar spectrum to create artificial measurements. 25 000 simulated exposures were created in this manner, and subsequently fitted with the templates. The scatter of the line centers over the series reveals the photon noise of the line positions. For comparison, an analogous simulation was done for the overlay of comb and Sun. Table 1 lists the results. The characteristic lines all have a photon noise in the low m/s range. The O<sub>2</sub> lines have particularly low photon noise, because they are quite deep and narrow. The overlaid comb increases the photon noise of the solar lines by 10 to 16 %. It is striking though, that for the O<sub>2</sub> lines the increase can be as low as 2 %. The reason is, that the O<sub>2</sub> lines are narrow enough to fit between the comb lines, where they are hardly affected by the comb’s photon noise. The impact of the comb is most pronounced if a comb line is located on the steepest slope of a line, which is most decisive for the localization of the line center.

#### 4.2. Tracking solar lines

We demonstrate the usefulness of our calibration methods by detecting signatures of global solar oscillations in our time series of disk-integrated solar spectra. Most of the power of these oscillations is concentrated at frequencies of about 3 mHz, which is why they are often referred to as the ”5-minute oscillations”. In integrated sunlight, only low-order oscillations with total velocity amplitudes of the order of 1 m/s are observed. Sensitive instruments with a stable wavelength calibration are required to detect these low-amplitude signals. Such global oscillations at a similar rate and amplitude are present in the spectra of other

stars, and have to be temporally averaged for the detection of low-mass exoplanets. The measurement of the well-explored global solar oscillations, whose detection has first been published in 1979 [17], serves as a proof-of-concept for our technique. Future applications may then investigate more contemporary problems such as the influence of sunspots on radial velocity detection, which is of great interest for high-sensitivity exoplanet searches.

For detecting the solar oscillations, we track the average shift of the three strong Fe I lines, which are the most distinct features from the Sun within the spectral range of our observation. Besides the solar lines, we also track the shifts of the O<sub>2</sub> lines imprinted by Earth’s atmosphere. These lines are often used as a low-precision reference, but are restricted to certain spectral regions. Their line centers are affected by Doppler shifts through changing wind speeds and directions. At noon, they are expected to be stable within a few m/s. This is because when the Sun is near the zenith, the winds are approximately perpendicular to the line of sight. During the course of the afternoon, however, the stability of the lines is supposed to degrade, as the component of the wind speeds along the line of sight increases.

Time traces of the average shifts of the four O<sub>2</sub> lines, and of the three Fe I lines, are shown in figure 9, both with time-interlaced and overlaid calibration. The time series is longer for the O<sub>2</sub> lines than for the Fe I lines, since for the tracking of the O<sub>2</sub> lines, telescope guiding problems can be tolerated. Over the course of the series, all four O<sub>2</sub> lines experience about the same drift of approximately  $-17$  m/s, similar to what found in earlier investigations [30, 31]. The largest portion of the drift is assumed to be caused by winds [30, 31], with a weaker contribution arising from the changing air-mass along the line of sight [31, 32]. Time-interlaced calibration confirms the results obtained with overlaid calibration, but with 2–3 times larger scatter. In the case of the overlaid spectra, the scatter is dominated by the measurement of the solar and telluric lines, rather than by the calibration. This limitation could be reduced by averaging a larger number of lines, e.g. with a spectrograph that records a wider spectral range.

The time traces of the Fe I lines, as shown in figure 9, display a strong drift from the rotation of the Earth, which needs to be subtracted. We do this by fitting and subtracting a second-order polynomial to the time traces, leading to the curves shown in figure 10 (a) and (c). This ”quick-and-dirty” way of accounting for Earth’s rotation is sufficient for the aim of detecting solar oscillations, and partly also compensates other unwanted effects such as differential extinction of the solar disc [18] and telescope guiding errors. Besides the expected 5-minute oscillations, the time traces also display a slower component, which is probably caused by guiding errors. The graphs on the right-hand side of figure 10 represent the power spectra of the time traces to their left, computed by FFT. The 5-minute oscillations are represented by a peak at 3.3 mHz in the power spectra. The frequency and the signal strength is in good agreement with the results reported in [17]. Our series of acquisitions is not long enough in time to fully resolve the substructure of the peak at 3.3 mHz. However, the weak side-lobes next to the central peak are likely to



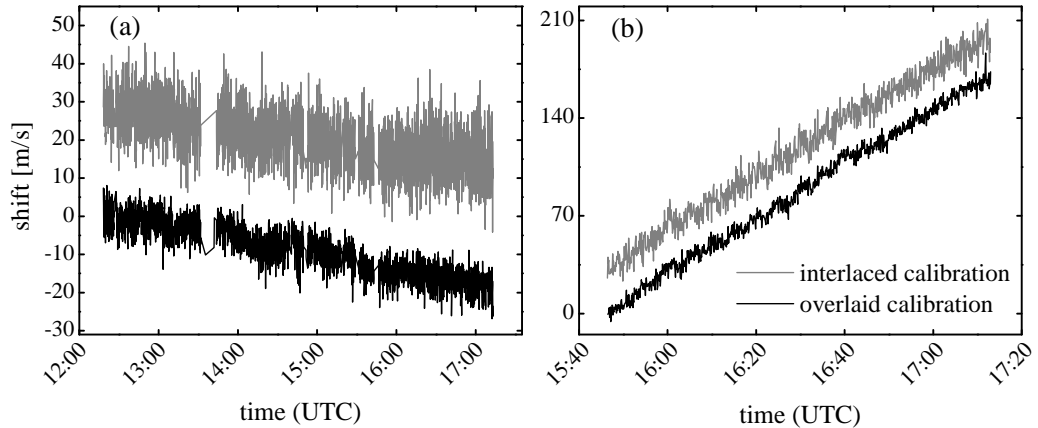


**Figure 9.** Tracking lines in the solar spectrum using time-interlaced calibration (gray lines) and overlaid calibration (black lines). For clarity, the gray lines were given a vertical offset relative to the black lines. (a) Shift of the telluric lines with time, averaged over four  $O_2$  lines. (b) Average shift of the three strongest Fe I lines.

stem from partly resolved oscillation modes. The total oscillation power of the central peak at 3.3 mHz corresponds to an amplitude of 88 cm/s. Amplitudes of the globally averaged solar oscillations have also been characterized in [19] using the HARPS spectrograph, where the strongest component is reported to have an amplitude of 25 cm/s, confirming earlier findings. Since in our measurements, the peak at 3.3 mHz contains numerous unresolved components, our results are in unison with this. Supposed errors from telescope guiding appear below 1 mHz. It is not clearly seen in the power spectrum obtained from time-interlaced calibration, probably because it interferes with noise.

The peak detection threshold with time-interlaced and overlaid calibration can be estimated by regarding the noise floor of the power spectrum. For an oscillation signal of unresolved width and a 3 sigma confidence level, it is of 37 cm/s for overlaid calibration. The calibration tests in section 3 yielded somewhat lower values with this scheme, but there only the standard deviation was specified, corresponding to merely 1 sigma. The guiding errors deteriorate the sensitivity of the measurement only at frequencies of below 1 mHz, where a signal would be masked by the guiding errors if its amplitude is below 63 cm/s. For time-interlaced calibration, the 3 sigma peak-detection threshold amounts to 69 cm/s. The performance is better than in section 3 because of the higher frame rate, and because considering the time series through a frequency filter is a way of applying a temporal average.

On the time scale of the oscillations, the  $O_2$  lines are relatively stable, and can thus also be used as a reference for their detection. Figure 10 (e) and (f) shows the analysis of the time trace of the Fe I lines as referenced to the  $O_2$  lines. All findings derived from comb calibration are confirmed. Due to the lower photon noise, the 3 sigma peak detection

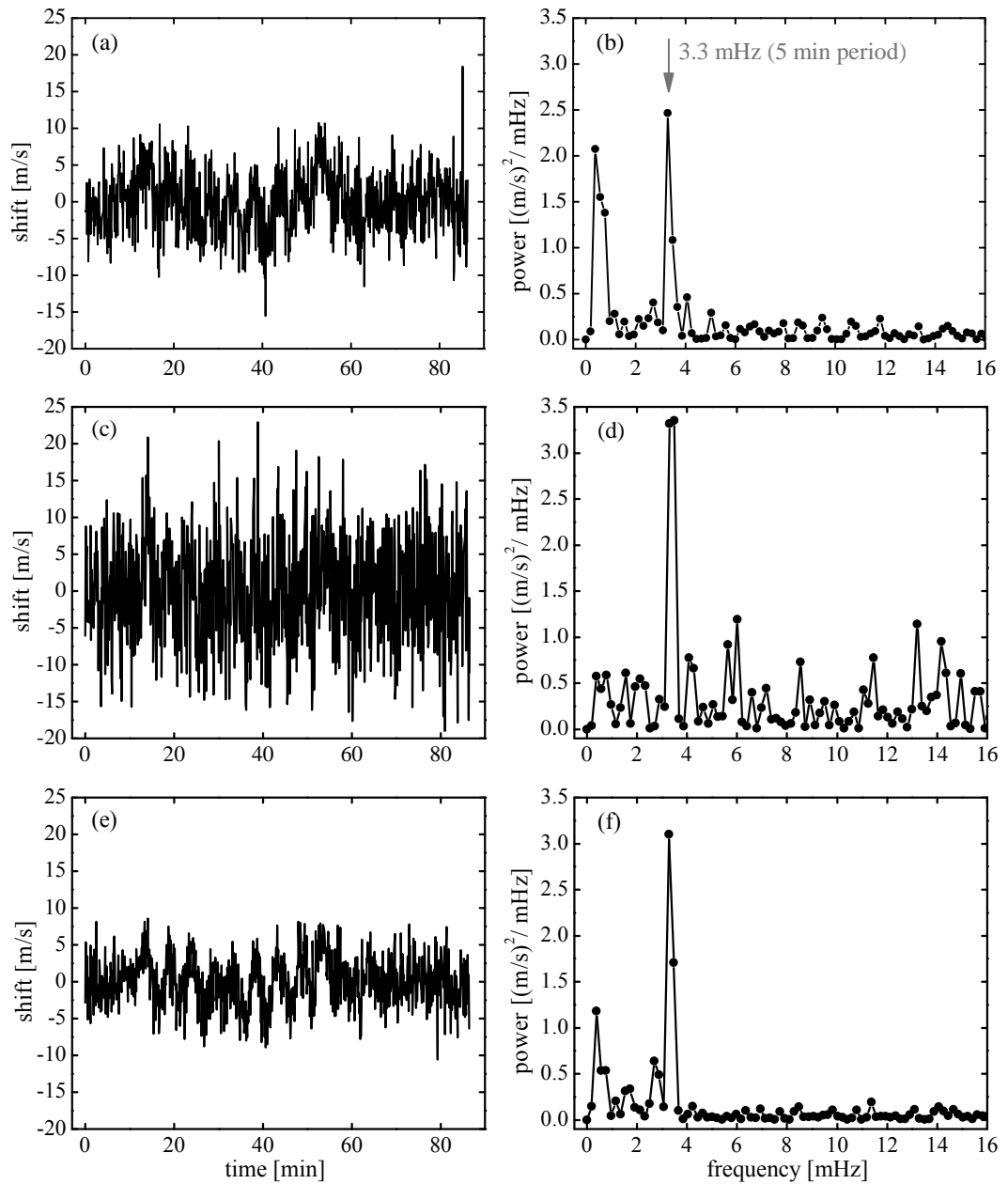


**Figure 10.** Detection of solar oscillations using the three strongest Fe I lines of figure 7 / table 1. Graphs on the left: Time traces with a second-order polynomial subtracted. Graphs on the right: Power spectra computed by fast Fourier transformation of the time traces. Note that these spectra scale quadratically in amplitude. Top: Overlaid calibration. Center: Time-interlaced calibration. Bottom: Calibration with telluric O<sub>2</sub> lines.

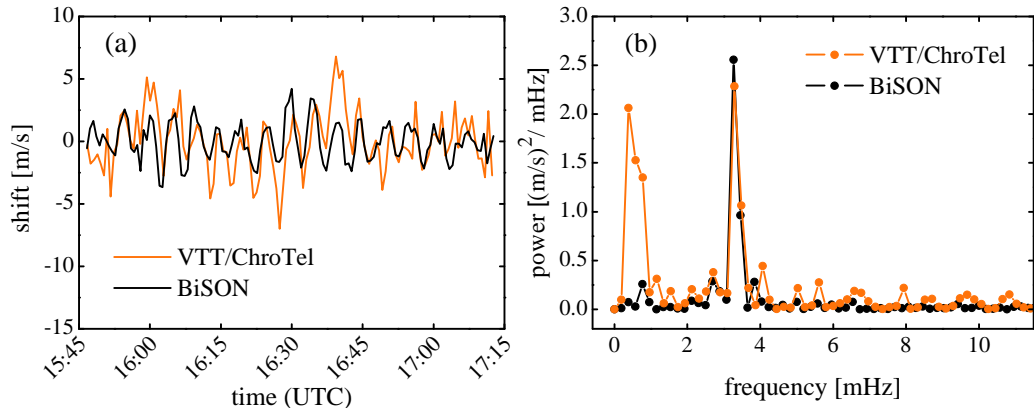


**Figure 11.** Comparison of solar oscillation measurements from VTT/ChroTel to BiSON data of the same date and time. The VTT/ChroTel data were calibrated with the overlaid comb. Additionally, the time series was binned over 7 exposures (42 s), to match the temporal resolution of the BiSON data (40 s). (a) Time series of RV shifts. (b) Power spectra, computed by fast Fourier transformation.

threshold is of 28 cm/s. Our above analysis however clearly reveals that over longer time frames, the  $O_2$  lines are unstable even on the 10 m/s scale, and are thus unsuited for sensitive detection of phenomena that occur on longer time horizons.

Disk-integrated solar oscillations have been measured for more than 3 decades by BiSON [18]. BiSON is a network of telescopes that observe solar oscillations via resonant scattering of a potassium line. This is a method very different from ours, which makes a comparison between the two all the more interesting. BiSON publicly provides data that also cover the time period of our observation. To these data, we compare our observation using overlaid calibration with the LFC. We bin our data over 7 exposures (42 s), to match the temporal resolution of the BiSON data (40 s). The comparison is shown in figure 11. The measured phases of the oscillations nicely match each other. Also the overall powers of the 5-minute oscillations agree within the expected uncertainties. The most obvious differences come from the guiding errors in our data, that appear at frequencies below 1 mHz. More subtle differences might arise from the different weighting of the solar limb in our observation.

## 5. Conclusion

We have demonstrated two LFC-assisted spectrograph calibration schemes, that both make use of a multiplexed SMF: Time-interlaced calibration, where the calibration and the measurement are separated in time, and overlaid calibration, where comb light is superimposed with light from the telescope. The latter technique has proven to be superior due to its simultaneous spatial mode matching between comb and sunlight. This approach

was found to be practical and very useful, but came at the expense of a more complex data analysis and of a slightly increased noise level. We could demonstrate a calibration repeatability down to better than 3.0 cm/s, paralleling the so far best results from the LFC on the HARPS spectrograph of 2.5 cm/s [9]. The use of SMFs brings in the additional benefit of eliminating modal noise as present in multimode fibers. With the proof-of-principle demonstration in this work, consisting of solar oscillation detection in disk-integrated sunlight, and of tracking of telluric lines, the concept is now ready for exploring physical phenomena on the Sun.

In astronomy, frequency combs are still a novelty and non-standard equipment at observatories. This however, is about to change, and LFC-assisted spectroscopy is envisioned to have a flourishing future in astronomy. Our present work shows how future astronomical LFCs could be utilized. Other observatories might consider a multiplexed fiber delivery, although employing multimode fibers. With further progress in adaptive optics, or by making use of astrophotonic devices such as photonic lanterns, future instruments might use multiplexed SMFs on stars other than the Sun, e.g. for exoplanet searches.

## Acknowledgments

We gratefully acknowledge the help of Frank Grupp from the University Observatory Munich, who has supported us with helpful discussions and advice. The KIS contribution to this project was in part funded by the Leibniz-Gemeinschaft within the "Pakt für Forschung und Innovation". The VTT is operated by the KIS at the Observatorio del Teide of the Instituto de Astrofísica de Canarias in Tenerife, Spain. LW is supported by the Forschungsprojekt GZ 788 of Chinesisch-Deutsches Zentrum für Wissenschaftsförderung, and the Young Researcher Grant of National Astronomical Observatories, Chinese Academy of Sciences. We thank the BiSON team (funded by UK Science, Technology and Facilities Council, STFC) for their friendly permission to use the time series of BiSON RV measurements. We also thank the technical staff of the VTT for their assistance.

## References

- [1] Udem Th, Holzwarth R, and Hänsch T W 2002 *Nature* **416** 233–237
- [2] Murphy M T *et al.* 2007 *Mon. Not. R. Astron. Soc.* **380** 839–847
- [3] Steinmetz T *et al.* 2008 *Science* **321** 1335–1337
- [4] Wilken T, Lovis C, Manescau A, Steinmetz T, Pasquini L, Lo Curto G, Hänsch T W, Holzwarth R, and Udem Th 2010 *Mon. Not. R. Astron. Soc.* **405** L16–L20
- [5] Ycas G G *et al.* 2012 *Opt. Express* **20** 6631–6643
- [6] Phillips D F *et al.* 2012 *Opt. Express* **20** 13711–13726
- [7] Doerr H P, Steinmetz T, Holzwarth R, Kentischer T and Schmidt W 2012 *Sol. Phys.* **280** 663–670
- [8] Doerr H-P, Kentischer T J, Steinmetz T, Probst R A, Franz M, Holzwarth R, Udem Th, Hänsch T W, and Schmidt W 2012 *Proc. SPIE* **8450** 84501G
- [9] Wilken T *et al.* 2012 *Nature* **485** 611–614

- [10] Molaro P *et al.* 2013 *A&A* **560** A61
- [11] Liske J *et al.* 2008 *Mon. Not. R. Astron. Soc.* **386** 1192–1218
- [12] Webb J K, King J A, Murphy M T, Flambaum V V, Carswell R F and Bainbridge M B 2011 *Phys. Rev. Lett.* **107**(19) 191101
- [13] Jovanovic N, Guyon O, Martinache F, Schwab C and Cvetojevic N 2014 *Proc. SPIE* **9147** 91477P
- [14] Betters C H, Leon-Saval S G, Robertson J G and Bland-Hawthorn J 2013 *Opt. Express* **21** 26103–26112
- [15] Spaleniak I, Jovanovic N, Gross S, Ireland M J, Lawrence J S and Withford M J 2013 *Opt. Express* **21** 27197–27208
- [16] Kosovichev A G 2009 *AIP Conf. Proc.* **1170** 547–559
- [17] Claverie A, Isaak G R, McLeod C P, van der Raay H B, and Roca Cortes T 1979 *Nature* **282** 591–594
- [18] Davies G R, Chaplin W J, Elsworth Y and Hale S J 2014 *Mon. Not. R. Astron. Soc.* **441** 3009–3017
- [19] Kjeldsen H, Bedding T R, Arentoft T, Butler R P, Dall T H, Karoff C, Kiss L L, Tinney C G and Chaplin W J 2008 *Astrophys. J.* **682** 1370–1375
- [20] Schröter E H, Soltau D and Wiehr E 1985 *Vistas Astron.* **28** 519–527
- [21] Bethge C, Peter H, Kentischer T J, Halbgewachs C, Elmore D F and Beck C 2011 *A&A* **534** A105
- [22] Kentischer T J, Bethge C, Elmore D F, Friedlein R, Halbgewachs C, KnÄülker M, Peter H, Schmidt W, Sigwarth M and Streander K 2008 *Proc. SPIE* **7014** 701413
- [23] Steinmetz T, Wilken T, Araujo-Hauck C, Holzwarth R, Hänsch T W, and Udem T W 2009 *Appl. Phys. B* **96** 251–256
- [24] Probst R A, Steinmetz T, Wilken T, Hundertmark H, Stark S P, Wong G K L, Russell P St J, Hänsch T W, Holzwarth R, and Udem Th 2013 *Opt. Express* **21** 11670–11687
- [25] Braje D A, Kirchner M S, Osterman S, Fortier T and Diddams S A 2008 *Eur. Phys. J. D* **48** 57–66
- [26] Probst R A *et al.* 2014 *Proc. SPIE* **9147** 91471C
- [27] The HITRAN Database <http://www.cfa.harvard.edu/hitran/>
- [28] Press W H, Teukolsky S A, Vetterling W T and Flannery B P 2002 *Numerical Recipes in C++* (Cambridge University Press)
- [29] Mayor M *et al.* 2003 *The Messenger* **114** 20–24
- [30] Balthasar H, Thiele U and Wöhl H 1982 *A&A* **114** 357–359
- [31] Figueira P, Pepe F, Lovis C and Mayor M 2010 *A&A* **515** A106
- [32] Caccin B, Cavallini F, Ceppatelli G, Righini A and Sambuco A M 1985 *A&A* **149** 357–364